ICAS 2021 SHANG HAI
International Council of the Aeronautical Sciences
32nd Congress of the International Council of the Aeronautical Sciences
September 6-10, 2021 Pudong Shangri-La, Shanghai, China

Multipoint optimization of Transonic Natural Laminar Flow Nacelles

Chongyang Yan[1], Yufei Zhang[2], Meihong Zhang[3]

[1] Tsinghua University, Beijing, 100084, People's Republic of China
[2] Corresponding author, Tsinghua University, Beijing, 100084, People's Republic of China
[3] Shanghai Aircraft Design and Research Institute, Shanghai 201210, People's Republic of China

Abstract

A numeric optimization framework for the design of natural laminar flow (NLF) nacelles is established based on differential evolution algorithm combined with RBF surrogate model. The class/shape transformation method is used for the parameterization of the geometry, and the $\gamma - \widetilde{Re}_{\theta t}$ transition model is used for transition prediction. Single-point optimization in cruise conditions for axis-symmetric nacelles demonstrates approximately 36% chord length of laminar flow, with 2.1 counts (1count=0.0001) of drag reduction. Two-point optimization considering drag-divergence conditions demonstrates similar results, with a slightly shorter laminar region but more shock wave drag reduction. The trade off between laminar flow drag reduction and shock wave drag considering drag-divergence performances is discussed.

Keywords: Transonic; natural laminar flow; nacelle; multipoint optimization

1. Introduction

Drag reduction is crucial for civil aircraft design. Among many drag reduction technologies, laminar flow control reduces friction by extending the laminar region over the surface of the aircraft [1]. Typical laminar flow control technologies are natural laminar flow control (NLFC) [2][3], laminar flow control (LFC) [4][5] and hybrid laminar flow control (HLFC) [6][7]. NLFC maintains the laminar region on the surface of the aircraft by geometry shape design. On the other hand, Large bypass ratio turbofan engines are usually installed on civil airliners. The friction of the nacelle surface occupies a considerable amount in that of the whole aircraft [8]. Moreover, compared with airfoils, there are no requirements on lift or moment for the design of nacelles, which gives it more freedom to design [9]. Consequently, the realization of natural laminar flow drag reduction on the nacelle can be expected to obtain considerable benefits.

There have been many studies on the design and experiments of NLF nacelles. Experiments in wind tunnel or flight tests on NLF nacelle was conducted by Younghans et al. [10], E.C. Hastings et al. [11] and DLR [12][13], and they all obtained a certain length of laminar flow, which verifies the feasibility of NLF nacelles. Numeric designs were also implemented on NLF nacelles with different optimization methods, such as invert design method by R. Radespiel et al. [8], and particle swarm optimization with Kriging surrogate model by Xiaolong He et al [9], and discrete-adjoint method by Ramy Rashad et al [14]. Drag reduction of 1.5%-2.0% of the whole aircraft can be obtained in these studies, together with considerable extension of the laminar region.

However, there are still some problems remained for the optimization design of natural laminar flow nacelles. Typically, natural laminar flow requires a certain length of favorable pressure gradient (FPG), so there is usually a strong shock wave behind the FPG region. The trade off between the laminar range and wave drag should be discussed. Furthermore, the drag reduction effect of the NLF nacelle at a higher Mach number, such as drag-divergence conditions should be also carefully examined, and multipoint optimization is necessary.

The rest of this paper consists of the following parts. First, an aerodynamic optimization framework for the design of axis-symmetric nacelles is established. Then, a single-point optimization is carried out to minimize the aerodynamic drag of the nacelle in cruse condition. Finally, a two-point optimization is carried out to take consideration of the drag divergence characteristics. The optimization results are compared, and the main considerations of NLF nacelle design is

demonstrated.

2. Optimization Framework

2.1 Geometric modeling and computational grid

As shown in Figure 1, a typical nacelle consists of the fan cowl, the inlet, the nozzle external duct and the nozzle internal duct. Generally, the total drag of the nacelle can be separated into two parts: the inner drag of the engine and the aerodynamic (external) drag of the nacelle. The laminar flow on the fan cowl aims at the reduction of the aerodynamic drag, and the other parts of the nacelle mainly affect the inner drag of the engine. As a result, the optimization design in this paper is focused on the geometric shape of the fan cowl.

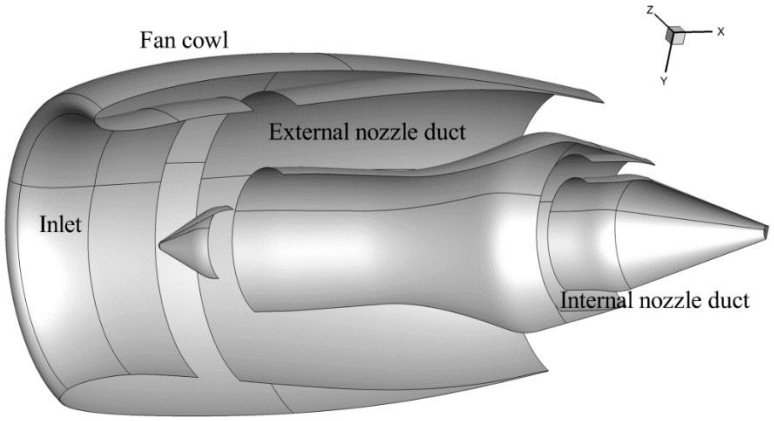

Figure 1 – A typical nacelle consisting of fan cowl, inlet and nozzle.

The geometric parameterization of the fan cowl is based on the class/shape transformation (CST) method [15], which can be used to generate a 2-dimensional profile. Generally, CST modeling consists of two steps. First, given a set of parameters $a_1, a_2, \ldots, a_n$, generate a standardized CST curve:

$$r = x^{n_1}(1-x)^{n_2}\sum_{k=1}^{n} a_k \frac{n!}{k!(n-k)!} x^k (1-x)^{n-k} \quad (1)$$

where n is the number of CST parameters (n=7 in this paper), and n_1,n_2 are the parameters related with the class function(n_1=0.5, n_2=2.0 in this paper).

Second, according to the actual location of the profile, scale the standardized CST curve linearly to the actual size.

For an axis-symmetric nacelle, the CST method generates the 2-dimensional profile of the fan cowl, and the whole fan cowl is obtained by sweeping the profile in circumferential direction.

The angle of attack for axisymmetric nacelles is set to 0°, so the geometric shape and the flow field are both axisymmetric, and the CFD calculation domain can be only a 30° sector of a cylinder to save computational cost. The grid for axisymmetric nacelles is shown in Figure 2. The heights of the first grid on the surface of the nacelle are about $5\times10^{-6}m$ to ensure $y^+<1$ on the wall, and the growth rate of the grid height are about 1.15. The total element number is about 51 thousand for the axisymmetric nacelle, and about 6.51 million for the non-axisymmetric nacelle. During the optimization, grid automatic generation is used with grid movement scripts.

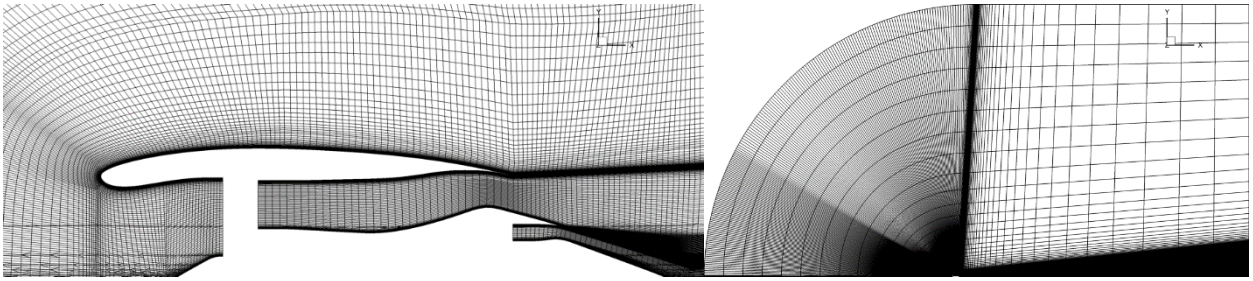

(a) Grid around the nacelle surface (b) Grid of the whole domain

Figure 2 – Grid for the non-axisymmetric nacelle.

2.2 Transition prediction method

Accurate transition prediction is important for natural laminar flow design. In this paper, the *SST-γ-Re$_{\theta t}$* transition model [16] is used for transition prediction. *γ-Re$_{\theta t}$* transition model is based on empirical correlation, which relates the freestream turbulent intensity *Tu* with the Reynolds number of momentum thickness at the transition position *Re$_{\theta t}$*. Apart from a modified SST model, two extra transport equations about intermittent factor γ and transition momentum thickness Reynolds number *Re$_{\theta t}$* need to be solved. The detail of the model equations can be found in [16]. The model has been tested on isolated nacelles and showed satisfying results compared with experiment data [17].

In this paper, the finite volume code CFL3D version 6.7[18] is applied for the Reynolds-averaged Navier-Stokes (RANS) computation. Airfoil NLR7301 is numerically computed to validate the accuracy of the *SST-γ-Re$_{\theta t}$* transition model [19]. The computational grid contains 79360 cells, as shown in Figure 3. The far field boundaries are 50 c (c is the chord length) away from the airfoil, and the first layer Δy^+<1 on the wall is ensured. The freestream condition is *Ma*=0.1 and *Re*=1.0×10^6. The freestream turbulence intensity is set to 0.3%. The computation results are shown in Figure 4, which are in good agreement with the experimental results.

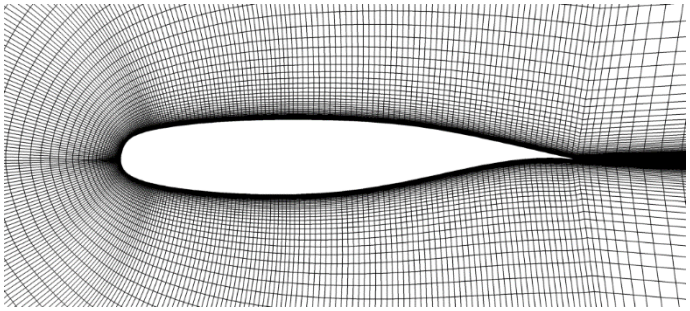

Figure 3 – The computation grid of the NLR7301 airfoil.

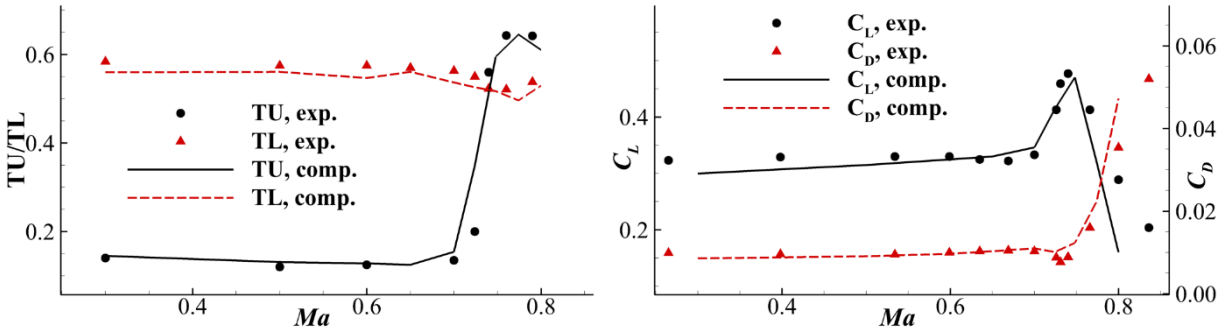

(a) Transition location (b) Lift coefficient and drag coefficient

Figure 4 – Comparison between computation and experiment.

Nacelles typically work at a certain condition in which the inlet mass flow rate keeps constant. In order to simulate the working condition of the nacelle, automatic mass flow rate control is used in the CFD computation. As shown in Figure 5, the static pressure at the ending section of the inlet is adjusted during the computation to reach the given inlet mass flow rate. For the internal and external nozzle ducts, the total pressure and total temperature at the starting sections of the nozzles are given as boundary conditions.

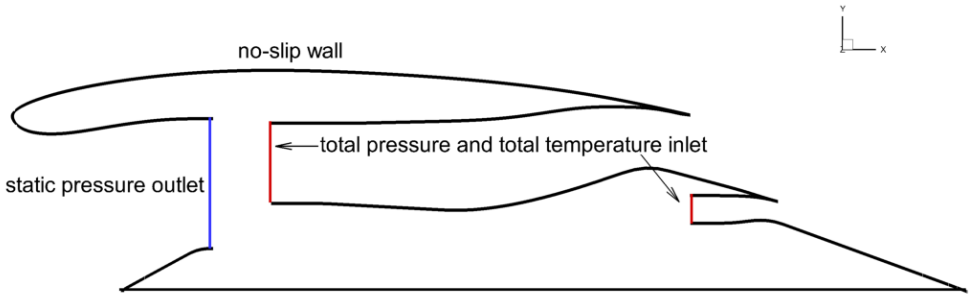

Figure 5 – Boundary conditions of the axisymmetric nacelle.

After the CFD computation, a thrust-drag bookkeeping method based on control volume integrations [20][21] is used to obtain the total drag of the nacelle, which is the difference between the ideal thrust and the net force on the nacelle. It should be noted that the total drag is not equal to the force on the nacelle wall obtained by CFD integration.

2.3 Optimization method

In this paper, an in-house developed hybrid optimization algorithm (HASADE) [22]is used for the optimization. The algorithm makes use of the strong global optimization ability of the differential evolution algorithm to ensure the diversity of the population, and in the meantime uses the radial basis function (RBF) response surface to strengthen the locally optimal search capability [23].

The Pressure distribution on the fan cowl is critical in the design of natural laminar flow nacelle. By adding some constraints on the pressure distribution based on the prior knowledge, the optimization process can be efficiently guided to the expected direction. Three pressure constraints are used in this paper, which are:

(1) The strength of shock wave S_{shock}, which is measured by the difference of pressure coefficient before and after the shock wave. In order to prevent excessive wave drag.

(2) The location where favorable pressure gradient disappears between 15%~70% chord length of the fan cowl x_{ftoa}. Generally this is around the location of transition.

(3) The maximum pressure coefficient gradient between 0~30% chord length of the fan cowl g_{cp}. This is used to control the magnitude of the favorable pressure gradient in the expected laminar flow region.

The optimization process is shown in Figure 6. The whole process can run automatically on the computer.

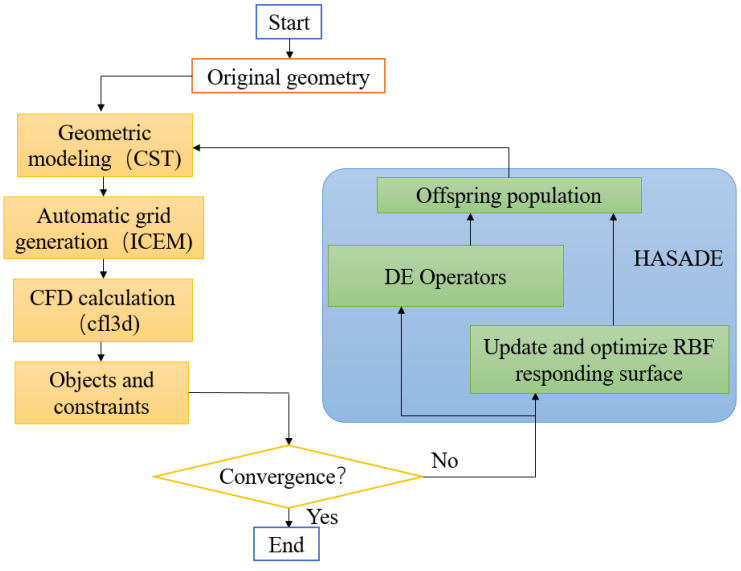

Figure 6 – The optimization process.

3. Optimization Design of Axisymmetric NLF Nacelle

3.1 Single-point optimization in cruise conditions

The optimization object is to minimize the pressure drag coefficient $C_{d,p}$ and the friction coefficient $C_{d,f}$ of the nacelle at the same time, which makes it a bi-object optimization problem. The length of FPG is constrained to be longer than 25% chord length of the fan cowl to ensure the existence of laminar flow. The optimization problem can be written as follow:

$$\begin{aligned} &\text{minimize} \quad C_{d,p}, C_{d,f} \\ &\text{s.t.} \quad \mathrm{Ma} = 0.85, \mathrm{Re} = 2.80 \times 10^7, C_m = 0.75, \alpha = 0° \\ &\begin{cases} S_{shock} < 0.6 \\ x_{ftoa} > 0.25 \end{cases} \end{aligned} \tag{7}$$

The convergence history of $C_{d,p}$ and $C_{d,f}$ is shown in Figure 7. The Pareto front of the two objectives are shown in Figure 8. The two branches of the Pareto front represents two classes of configurations, which will be discussed shortly. The optimal result is shown in Table 1. Compared to the original configuration, the total drag is reduced by 2.1counts, and the length of laminar flow reaches 38% chord length of the fan cowl from the original 29%. The distribution of pressure coefficient C_p and friction coefficient C_f on the fan cowl of the original and optimized nacelles are shown in Figure 9.

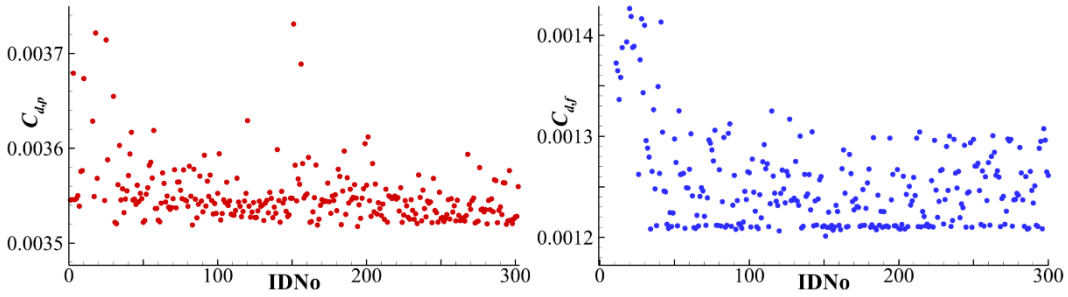

Figure 7 – The convergence history of $C_{d,p}$ and $C_{d,f}$.

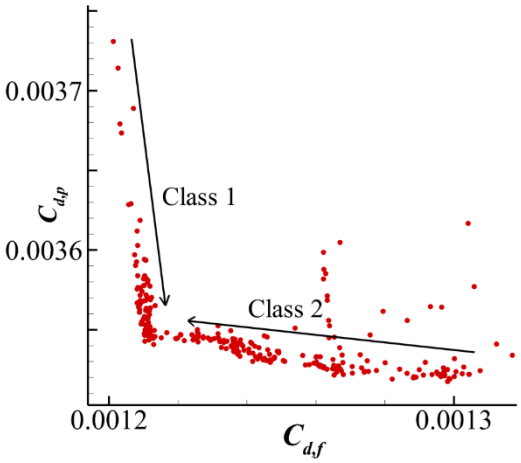

Figure 8 – The Pareto front of the two objectives.

Table 1 The optimal result of single-point optimization

	$C_{d,t}/10^{-4}$	$C_{d,f}/10^{-4}$	Relative length of laminar flow
original	25.5	13.0	29%
optimal	23.4	12.1	38%

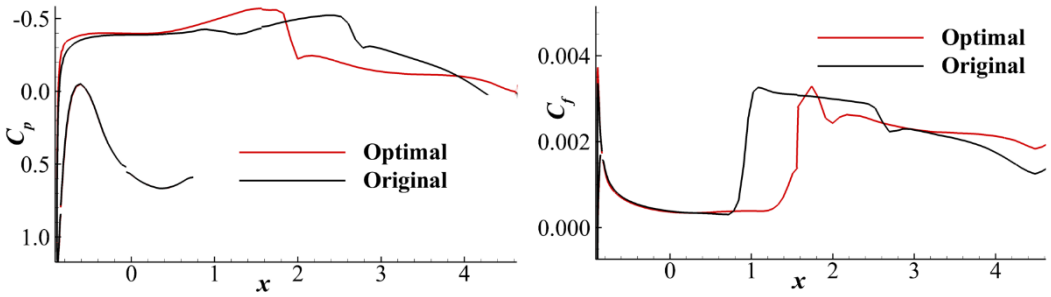

Figure 9 – The C_p and C_f distribution on the fan cowl of the original and optimized nacelles.

It's enlightening to study the aerodynamic characteristics of the individuals of the two classes in the Pareto front shown in Figure 8. For the individuals of the first class shown in Figure 10, when the length of laminar flow increases, the $C_{d,f}$ decreases rapidly while the $C_{d,p}$ grows slowly, so the overall effect of extending laminar flow is reducing the total drag of the nacelle. For the individuals of the second class shown in Figure 11, the length of laminar flow is long enough to make the shock wave strengthen rapidly, and the $C_{d,p}$ increases faster than the reduction of $C_{d,f}$ from the extending of laminar flow. Consequently, the optimal configuration to reduce the total drag lies in the trade-off point between these two classes of configurations, and this indicates the contradiction between the length of laminar flow and shock resistance.

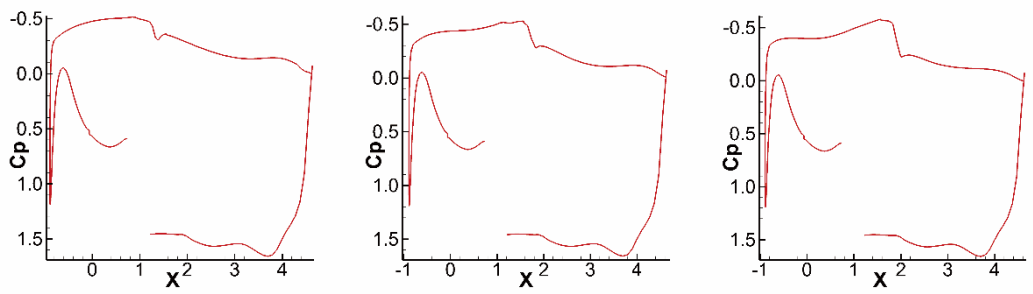

Figure 10 – The typical individuals in the first direction.

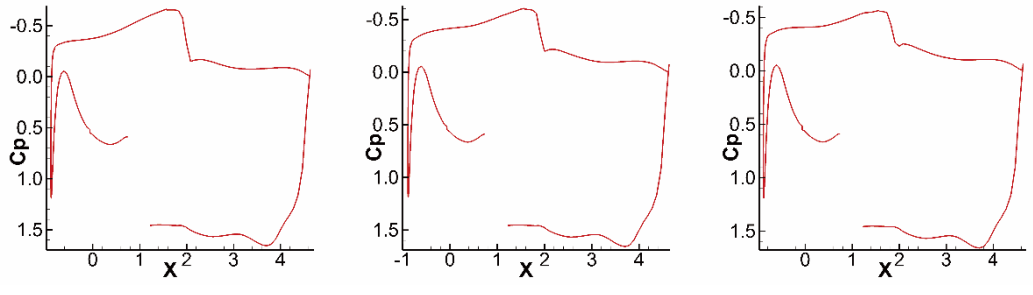

Figure 11 – The typical individuals in the second direction.

3.2 Two-point optimization in cruise and drag divergence conditions

The flight conditions for wide body aircrafts is changing during the whole flight mission. Besides cruise conditions, the performance in other typical flight conditions such as drag divergence, one engine failure (windmill) and large side slip angle should also be considered. For NLF nacelles, the shock wave drag offset the laminar flow drag reduction to some extent, so it's important to ensure that the drag reduction remains satisfying at a higher Mach number, when the shock wave becomes stronger. Consequently, the drag divergence condition is mainly considered in this paper.

The Mach number in drag divergence conditions is 0.87, and the other freestream states are the same as the cruise conditions. The optimization object is to minimize the $C_{d,t}$ in both cruise and drag divergence conditions simultaneously. The population size is 16, and the total generations are 30. The $C_{d,t}$ of all the individuals in cruise and drag divergence conditions is shown in Figure12. The

Pareto front shows that the drag reduction in drag divergence condition is negatively correlated with the drag in cruise condition.

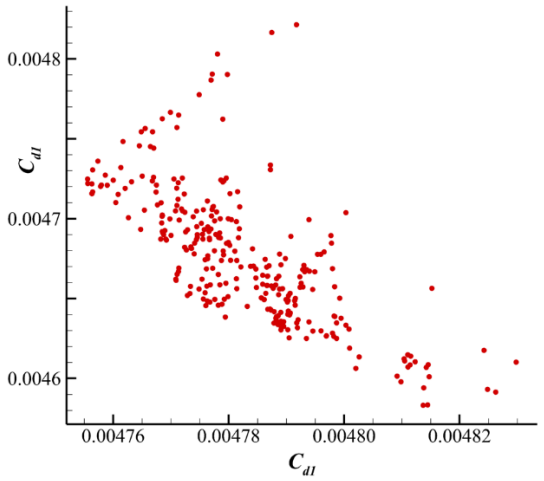

Figure 12 – The $C_{d,t}$ of all the individuals in cruise and drag divergence condition.

The performance of the optimal configuration is shown in Table 2. The distribution of C_p and C_f on the fan cowl in the two conditions are shown in Figure13. Compared with the cruise condition, the length of FPG as well as the location of shock wave moves downstream, and the shock wave is strengthened in drag divergence condition. This explains why the range of laminar flow is a little longer in drag divergence condition than in cruise condition. The rise of $C_{d,t}$ between the two conditions mostly comes from the shock wave drag.

Table 2 The performance of the optimal configuration of the two-point optimization

condition	$C_{d,t}$ /10^{-4}	$C_{d,f}$ /10^{-4}	Relative length of laminar flow
cruise	23.5	12.3	36%
Drag divergence	24.7	11.7	38%

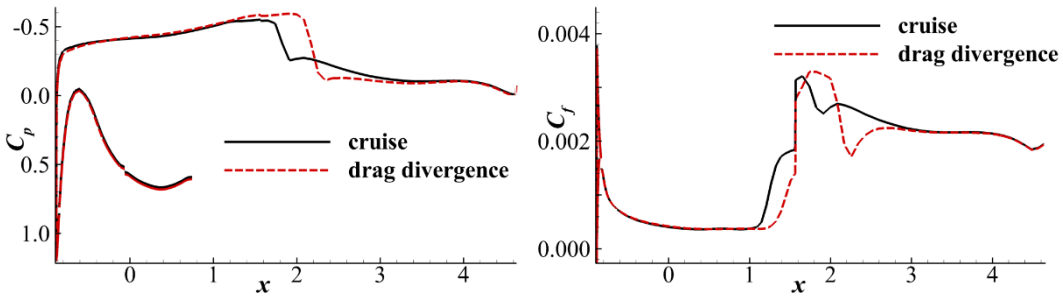

Figure 13 – The C_p and C_f contribution on the fan cowl in cruise and drag divergence conditions.

3.3 Comparative analysis of the two optimizations

The optimal configurations obtained from the single-point and two-point optimizations (referred to as OPT1 and OPT2) are compared to find the effects of drag divergence condition on the design of NLF nacelles. The C_p distributions of the fan cowl on OPT1 and OPT2 at cruise and drag divergence conditions are shown in Figure 14. The shock wave and the length of FPG are slightly weaken for OPT2, which means when considering drag divergence conditions, the shock wave drag is further reduced at the cost of slightly shortened laminar flow range. Figure15 shows the profiles of OPT1 and OPT2. The maximum diameter of the optimized NLF nacelle is reduced for a bit to waken the acceleration of flow as well as the shock wave strength.

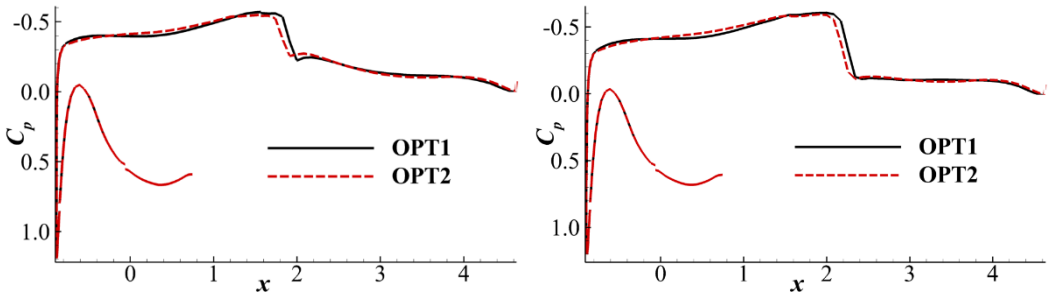

(1) Cruise condition (2)Drag divergence condition

Figure 14 – The C_p distributions of the fan cowl on OPT1 and OPT2 at cruise and drag divergence conditions.

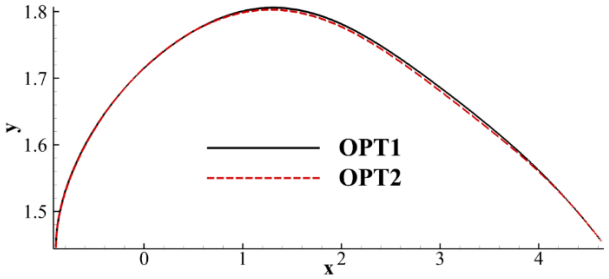

(1) Cruise condition (2)Drag divergence condition

Figure 15 – The optimal profiles of fan cowl in single-point and two-point optimizations.

The two optimized configurations are further computed at a serious of freestream Mach numbers to test the drag rise characteristics. The results are shown in Table 3. Compared to OPT1, the length of laminar flow on OPT2 is slightly shorter at cruise condition, and the $C_{d,t}$ is almost the same. However, at higher Mach numbers, the $C_{d,t}$ of OPT2 becomes lower than OPT1, which shows superior drag rise characteristics.

Table 3 The drag rise characteristics of the OPT1 and OPT2 nacelles

Ma	$C_{d,t}$ /10^{-4}		$C_{d,f}$/10^{-4}		Relative length of laminar flow	
	OPT1	OPT2	OPT1	OPT2	OPT1	OPT2
0.85	**23.4**	**23.5**	12.1	12.3	38%	36%
0.86	23.8	23.8	11.7	12.0	41%	36%
0.87	**25.1**	**24.7**	11.5	11.7	39%	38%
0.88	27.2	26.7	11.5	11.5	41%	41%
0.89	30.4	30.2	11.3	11.0	41%	41

4. Conclusions

In this paper, a numeric optimization framework is established for the design of NLF nacelle using differential evolution algorithm combined with RBF surrogate model. Cruise and drag divergence conditions are both considered, which makes it a multipoint optimization. Both single-point and two-point optimizations show extended laminar flow region and drag reduction.

Single-point optimization on axisymmetric nacelles shows that there is a contradiction between the length of laminar flow and wave drag. Under the freestream conditions in this paper, the optimal length of laminar flow is 38% chord length of the fan cowl, with 2.1 counts of drag reduction.

When considering drag divergence characteristics of axisymmetric NLF nacelles, the negative effects of wave drag increase and consequently the optimal length of laminar flow is slightly shortened. However, the optimized nacelle still has a considerable range of laminar flow, and even

though the slight increase of friction, the total drag is reduced at higher Mach numbers because of the reduction of wave drag.

Copyright Statement

References

[1] G Schrauf. Status and perspectives of laminar flow. Aeronautical Journal 2005;109(1102):639–44. Doi: 10.1017/S000192400000097X.

[2] Lynde, M. N. , R. L. Campbell . Computational Design and Analysis of a Transonic Natural Laminar Flow Wing for a Wind Tunnel Model. Aiaa Applied Aerodynamics Conference 2017.

[3] Z Han, J Chen, K Zhang, et al. Aerodynamic shape optimization of natural-laminar-flow wing using surrogate-based approach. AIAA Journal 2018;56(7):2579–93. Doi: 10.2514/1.J056661.

[4] J Mount, V Millman. Development of an Active Laminar Flow Nacelle. AIAA Paper 1985-1116 1985. Doi: 10.2514/6.1985-1116.

[5] S Chernyshev, M Gamirullin, V Khomich, et al. Electrogasdynamic laminar flow control on a swept wing. Aerospace Science and Technology 2016;59:155–61. Doi: 10.1016/j.ast.2016.10.019.

[6] K Krishnan, O Bertram, O Seibel. Review of hybrid laminar flow control systems. Progress in Aerospace Sciences 2017;93(June):24–52. Doi: 10.1016/j.paerosci.2017.05.005.

[7] Y Wie, F Collier, J Viken, et al. Design of a hybrid laminar flow control engine nacelle. AIAA Paper 1992-0400 1992. Doi: 10.2514/6.1992-400.

[8] R Radespiel., K Horstmann, G Redeker. Feasibility study on the design of a laminar flow nacelle. Journal of Aircraft 1990;27(11):959–65. Doi: 10.2514/3.45966.

[9] X He, J Bai, X Lu, et al. Natural laminar flow nacelle optimization design based on EFFD method. Journal of Aerospace Power 2014;29(10):2311–20. Doi: 10.13224/j.cnki.jasp.2014.10.006.

[10] J Younghans, D Lahti. Analytical and Experimental Studies on Natural Laminar Flow Nacelles. AIAA Paper 1984-0034 1984. Doi: 10.2514/6.1984-34.

[11] E Hastings, J Schoenster, C Obara, et al. Flight Research on Natural Laminar Flow Nacelles: A Progress Report. AIAA Paper 1986-1629 1986. Doi: 10.2514/6.1986-1629.

[12] H Riedel, K Horstmann, A Ronzheimer, et al. Aerodynamic Design of a Natural Laminar Flow Nacelle and the Design Validation by Flight Testing. Aerospace Science and Technology 1998;2(1):1–12. Doi: 10.1016/S0034-1223(98)80001-8.

[13] H Riedel, A Ronzheimer, M Sitzmann. Analysis of the Static Pressure Distribution on a Laminar Flow Nacelle Based on Euler Calculations and Flight Measurements. Aerospace Science and Technology 1998;2(2):129–43. Doi: 10.1016/S0034-1223(98)80011-0.

[14] R Rashad, D Zingg. Aerodynamic shape optimization for natural laminar flow using a discrete-Adjoint approach. AIAA Journal 2016;54(11):3321–37. Doi: 10.2514/1.J054940.

[15] M Albert, D Bestle. Automatic design evaluation of nacelle geometry using 3D-CFD. AIAA AVIATION 2014 -15th AIAA/ISSMO Multidisciplinary Analysis and Optimization Conference 2014;(June):1–9. Doi: 10.2514/6.2014-2039.

[16] F Menter, R Langtry, S Likki, et al. A Correlation-based Transition Model Using Local Variables—Part 1: Model Formulation. Journal of Turbomachinery 2006;128:413–22. Doi:10.1115/1.2184352

[17] Y Lin, T Robinson, J Early, et al. Implementation of Menter's transition model on an isolated natural laminar flow nacelle. AIAA Journal 2011;49(4):824–35. Doi: 10.2514/1.J050890.

[18] "CFL3D Version 6 Home Page." Https://Cfl3d.Larc.Nasa.Gov/. n.d.

[19] "NLR 7301 Airfoil," Experimental Data Base for Computer Program Assessment, AGARD Rept. AR-138, Neuilly sur Seine, France, 1979.

[20] J Joo, T Tillman, R Lin. Nacelle External Drag prediction using Computational Fluid Dynamics. 48th AIAA/ASME/SAE/ASEE Joint Propulsion Conference and Exhibit 2012;(August):1–25. Doi: 10.2514/6.2012-3998.

[21] Y Zhang, H Chen, S Fu, et al. Drag prediction method of powered-on civil aircraft based on thrust drag bookkeeping. Chinese Journal of Aeronautics 2015;28(4):1023–1033. Doi: 10.1016/j.cja.2015.06.015

[22]K Deng, H Chen. Hybrid Optimization Algorithm based on Differential Evolution and RBF Response Surface. Chinese Journal of Theoretical and Applied Mechanics 2017;49(2):441–55. Doi: 10.6052/0459-1879-16-285.

[23]C Smith, W Crossley. Investigating response surface approaches for drag optimization of a subsonic turbofan nacelle. 8th Symposium on Multidisciplinary Analysis and Optimization 2000;(c). Doi: 10.2514/6.2000-4797.